Physics of the Solid State, 2025, Vol. 67, No. 2

12,05

Magnetic $NiFe_2O_4$ Nanoparticles Functionalized for Magnetic Powder Imaging (MPI)

© *A.S. Kamzin*[1], *N. Dogan*[2], *L.S. Kamzina*[1], *A.V. Kopylov*[3]

[1] Ioffe Institute,
St. Petersburg, Russia
[2] Department of Physics, Gebze Technical University,
Kocaeli, Turkey
[3] JSC „RITVERTs“,
St. Petersburg, Russia
E-mail: ASKam@mail.ioffe.ru

Received February 10, 2025
Revised February 12, 2025
Accepted February 12, 2025

The properties of $NiFe_2O_4$ magnetic nanoparticles (MNPs) synthesized by the hydrothermal method, as well as the dependence of the properties on the functionalization (coating) of the particles with citric or polyacrylic acids by the coprecipitation method are studied. The properties of the obtained MNPs are studied by X-ray diffractometry (XRD). The magnetic properties of the samples and the phase state of the MNPs are studied using the physical property measurement system (PPMS) and Mössbauer spectroscopy. It is found that when $NiFe_2O_4$ MNPs are functionalized, citric or polyacrylic acids cover individual particles with shells, which reduces segregation and interaction of MNPs with each other, as a result of which the nanoparticles acquire superparamagnetic properties, which is extremely necessary for the latest technique of magnetic powder visualization of human organ diseases.

Keywords: $NiFe_2O_4$ ferrite-spinel magnetic nanoparticles, hydrothermal synthesis, functionalization with citric or polyacrylic acid, magnetic properties, magnetic structure, magnetic powder imaging.

DOI: 10.61011/PSS.2025.02.60687.29-25

1. Introduction

This publication further develops the works focused on creation and investigation of magnetic nanoparticles (MNP) [1–6] for applications in a new unique and powerful magnetic-particle imaging (MPI) method used for diagnosis of diseases. The idea and fundamentals for the development of MPV technology as a tomographic radiation-free high-sensitivity imaging method were first described in 2001 [7]. The first scanner for direct tomographic MPV *in vivo* imaging with high resolution of spatial distribution of superparamagnetic MNP (SPMNP) is described in [8]. The first MPI demonstration with quick visualization in a wide field of view was carried out in 2010 [9]. There is currently a number of reviews addressing MPI [10,11].

MPI-specific *in vivo* MNP or tracers with the following fundamental properties serve as a source of imaging signal for the MNP scanner: (1) residual magnetization of MNP shall disappear after disabling of the external excitation magnetic field; (2) MNP magnetization curve shall be nonlinear; (3) MNP shall have magnetic saturation to distinguish the MNP signal from the excitation field signal; (4) the employed MNP shall be in a superparamagnetic state [12–16]. However, spatial resolution and sensitivity of MPI also depend on the MNP properties such as diameter, magnetic moment and magnetization curve slope of a particle [1–6,15–20]. Thus, formation of MNP with desired properties is a vital task for magnetic particle imaging of organs.

However, MNP must not be introduced into a living body because human body fluids (blood, etc.) biochemically easily recognize viruses, bacteria, etc., as well as foreign matter, which are later passivated by the immune system. Moreover, MNP are often toxic and biologically incompatible. To avoid such negative effects, MNP are coated with biologically compatible material and introduced into a living body in the form of a magnetic suspension consisting of MNP dispersed in liquid. This poses new requirements for biomedical MNP such as stability, high colloidality, absence of agglomeration, etc. As a consequence, core-shell MNP occurred, in which the core consisted of MNP with high magnetic properties and the shell consisted of biologically compatible materials: polyethyleneglycol, polyethyleneimine, dextran, biologically compatible iron oxides, citric acid, polyacrylic acid, graphene oxide, chitosan, etc. [1–6,15–21]. Shells might be made of various materials and serve not only for environmental protection of the particle and agglomeration prevention in a similar way to organic or inorganic material coatings. **Surface modification** — is MNP coating with chemical groups or molecules such as hydroxyl or carboxyl groups. **Surface functionalization** — is MNP surface coating with biological molecules. These methods improve MNP stability, but require control of magnetic property variations due to the presence of a shell.

Thus, the objective of this work was to develop a technology of fabricating $NiFe_2O_4$ MNP and further coating of MNP with polyacrylic ($NiFe_2O_4$@PAA) and citric ($NiFe_2O_4$@CA) acids and optimization of MNP properties for utilization in MPI. Spinel $NiFe_2O_4$ was chosen because they are non-toxic and this attracts the attention of researchers due to the opportunity of biomedical applications [1,21–27].

Polyacrylic acid (PAA) was chosen due to its high biocompatibility, solubility in water and greater amount of polyacrylic acid groups for formation of chelates with mixed cations. PAA coating prevents MNP agglomeration and renders hydrophilic properties to particle surfaces. High density of reactive functional groups in PAA makes it attractive for biomedical applications [1,28–30].

Citric acid (CA) is a biologically active substance that exerts a number of positive effects on the body, for example, antibacterial effect, immune stimulation, anticarcinogenic and cleaning (removes toxins) effects, and normalizes the endocrine system [3,31,32]. CA is chemisorbed on iron oxide MNP forming a carboxylate group with Fe−OH groups on the particle surface, leaving negatively charged carboxyl groups, to which drugs may be bonded for target delivery into the body. The novelty of this study is in obtaining data about the effect of polyacrylic or citric acid coating on magnetic properties of $NiFe_2O_4$ MNP.

2. Experimental methods

2.1. Materials

Materials for synthesizing $NiFe_2O_4$ MNP, i.e. $FeCl_2 \cdot 4H_2O$, $FeCl_3 \cdot 6H_2O$, $NiCl_2$ and NH_4OH (25% ammonia) were made by Sigma Aldrich with 99% purity, without additional purification. Citric acid (CA) monohydrate and polyacrylic acid (PAA), Sigma Aldrich, were used for coating the synthesized $NiFe_2O_4$ MNP.

2.2. $NiFe_2O_4$ MNP synthesis and polyacrylic acid coating

Among the known methods of synthesizing $NiFe_2O_4$ MNP (co-deposition, microwave combustion, sol-gel self-ignition, etc.), hydrothermal method was used to perform controlled particle synthesis with desired magnetic properties. However, this method needs correction to limit the growth at the stage of quasi spherical high-crystallinity particles by controlled size and shape [1,13,33].

$NiFe_2O_4$nanoparticles were synthesized by the hydrothermal technique. For this, 6 mmol of $FeCl_3 \cdot 6H_2O$ and 3 mmol of $NiCl_2$ were dissolved in 40 ml of distilled water. The obtained mixture was stirred using a mechanical stirrer at a rate of 500 revs/min at room temperature during 2 min in nitrogen, and then stirred again during 3 min after addition of 5.5 ml 25% NH_4OH solution in water to the mixture. The solution was placed in an autoclave with PTFE seal and held at 250°C for 12 hours. Then, the autoclave was cooled down to room temperature in air. Extracted sediment was washed three times in distilled water and separated in a strong permanent magnet field. The prepared particles were dried in furnace at 65°C.

The surface of $NiFe_2O_4$ particles was coated with polyacrylic (or citric) acid using the co-deposition technique. For this, a solution was prepared from 50 ml of deionized water and 3 mmol of polyacrylic (or citric) acid and the synthesized $NiFe_2O_4$ MNP were added to this solution. The mixture was stirred in an ultrasonic bath at 65°C. Then 1 ml of NH_4OH solution in water was added dropwise and stirred mechanically during 30 min in nitrogen flow to prepare core-shell MNP. Nitrogen flow was stabilized in tis process to protect against environmental factors and agglomeration effect. The MNP were washed with distilled water and then dried in a furnace at 60°C during 2 h.

2.3. Research methods

Various techniques were used to study the properties of synthesized MNP. Thus, X-ray diffraction patterns were made using the Rigaku Dmax 2200 diffractometer with $\lambda = 0.154$ nm Cu-K_α radiation (at 40 kW and 35 mA) in the diffraction angle range from 10 to 90° (2θ) in 0.02° scanning steps. To confirm that there are functional groups of PAA and CA (coatings) on the $NiFe_2O_4$ MNP surface, Fourier transform infrared spectra were recorded using the Perkin Elmer L160000R FTIR spectrometer with a multipurpose total internal reflection module [1]. Magnetic parameters of the synthesized MNP (saturation magnetization (M_s), coercive field (H_c) and residual magnetization (M_r)) were measured using the Quantum Design Model 6000 system.

Magnetic properties and phase state of the synthesized MNP were studied by Mössbauer spectroscopy that can unambiguously identify iron-containing phases in samples (which is unattainable by other methods), because this technique is highly sensitive to hyperfine nuclear interactions [33–37], Mössbauer spectra (MS) of the synthesized MNP were recorded with detection of gamma-ray from Co^{57}(Rh) source with sample transmission configuration. Velocity scale was calibrated using 6 mkm α-Fe foil at room temperature. Experimental MS were processed mathematically using a specialized program [38], which describes the spectral lines by the Lorentz-shape peaks using the least-square method. The program [38] was also used to recover the distribution probabilities of effective magnetic fields (H_{eff}) from the experimental MS. A discrepancy between the model representations of the recorded MS and experimental data is determined by statistic deviations. In the procedure for minimizing the functional χ^2, the program searches for optimum widths, intensities and spectral line positions. Using the spectral line positions on the velocity scale, the program calculates ultrafine interaction (UFI) parameters: IS — isomeric shift of Mössbauer lines, QS — quadrupole splitting, H_{eff} — effective magnetic field.

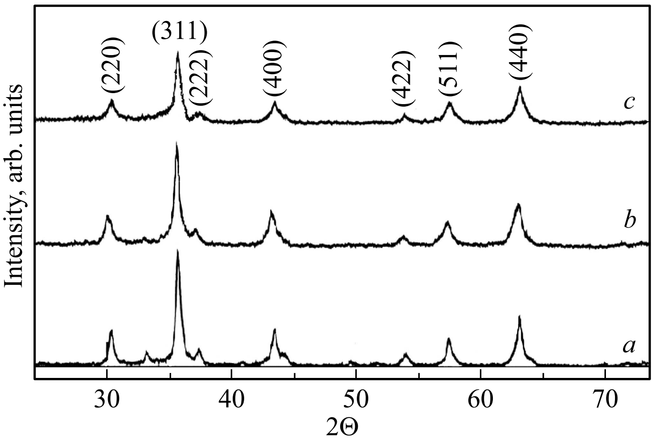

Figure 1. X-ray diffraction patterns of MNP (*a*) — $NiFe_2O_4$, (*b*) — $NiFe_2O_4$@CA and (*c*) — $NiFe_2O_4$@PAA.

3. Experimental data and analysis

3.1. X-ray diffraction examination results

Experimental X-ray diffraction patterns (XRD) of the synthesized $NiFe_2O_4$ MNP without and with polyacrylic and citric acid coating are shown in Figure 1. The shown X-ray images for each sample contain typical peaks (220), (311), (400), (422), (511) and (400) at 2Θ of 30.4°, 35.7°, 38.0°, 43.5°, 54.1°, 57.5° and 63.1°, respectively, related to the crystalline phase of cubic nickel spinel with the lattice constant $a = 8.4 \pm 0.1$ Å, which agrees well with the literature data (card JCPDS № 89–1012, $a = 8.433$ Å) [39–42]. Note that the diffraction lines of the examined particles are broadened compared with the macrocrystal lines, which confirms the nanoscale dimensionality of crystallites in the examined powders. For coated samples, a decrease in diffraction line intensities and widths is observed. Mean crystallite sizes D (nm) were calculated using maximum intensity line (311) from reflection plane (311) using the Debye–Scherrer equation (see [43] and references therein):

$$D = \frac{K\lambda}{\beta \cos\theta}, \qquad (1)$$

here, λ is the Cu-K_α (1.5418 Å) X-ray radiation wavelength, K is the Scherrer constant (0.89), β is the full width at half maximum of diffraction line intensity, and θ is the line angle. Calculated D (nm) for $NiFe_2O_4$, $NiFe_2O_4$@CA, $NiFe_2O_4$@PAA MNP were 10.0 nm, 11.6 nm and 12.9 nm, respectively, which differed a little from those calculated in [1]. $NiFe_2O_4$ MNP sizes increase with increasing coating material density.

Such parameters as lattice constant (a), dislocation density (δ) and specific surface area (S) of the examined MNP were calculated using the equations given in [1] and similar results were obtained. In the uncoated $NiFe_2O_4$ sample, large clusters are formed due to strong interactions, and act as single particles. Therefore, the lattice parameter of uncoated$NiFe_2O_4$ MNP is larger than that of coated particles.

Table 1. MNP sizes, lattice constants and structural parameters of $NiFe_2O_4$ MNP depending on the type of coating

Sample	D (nm)	a (nm)	ρ (g/cm^3)	δ (10^{15} m^{-2})	S (10^4 m^2/g)
$NiFe_2O_4$	10.0	8.43	5.15	10.12	11.75
$NiFe_2O_4$@CA	11.6	8.37	5.25	6.77	9.20
$NiFe_2O_4$@PAA	12.9	8.28	5.35	6.37	9.10

3.2. Mössbauer spectrometry of $NiFe_2O_4$, $NiFe_2O_4$@PAA and $NiFe_2O_4$@CA MNP

Advantages of the Mössbauer spectroscopy are in reliable detection of phase composition, ion distribution over non-equivalent position, magnetic structure, percentage of iron compounds and hyperfine interactions in iron-containing materials [2–6,17–20,28,33–37,42,44–46]. This is due to the abilities of the Mössbauer spectroscopy to identify unambiguously iron oxides, which is unattainable for other methods.

Mössbauer spectra (MS) measured at room temperature (300 K) of $NiFe_2O_4$ MNP and functionalized $NiFe_2O_4$@PAA and $NiFe_2O_4$@CA MNP are shown in Figure 2, *a*. Dots on the MS (Figure 3, *a*) indicate experimental data. Effective magnetic field distribution probability functions $P(H_{\text{eff}})$ calculated from experimental MS (Figure 2, *a*) are shown in Figure 2, *b*. MS of $NiFe_2O_4$ macocrystals [26,44,45] differ considerably from those shown in Figure 2, *a*. As the sizes decrease, $NiFe_2O_4$ MNP MS take a relaxation form (see, for example, [28,29,42,45–48]), similar to MS shown in Figure 2, *a*.

An important property of magnetic nanoparticles that is necessary for MPI is the superparamagnetic state that occurs at small MNP sizes when heat energy overcomes the particle anisotropy energy and the magnetization orientation skips its direction from the orientation of one easy axis to another [47], which complicates the analysis of MNP MS considerably (Figure 2, *a*). Therefore, mathematical processing of the experimental $NiFe_2O_4$ MNP MS also used a complex procedure of fitting and recovery of $P(H_{\text{eff}})$ from MS using the program [38]. The $P(H_{\text{eff}})$ recovery process involves: (1) a set of sextuplets whose relaxation times exceed the Mössbauer experiment time window limit (10^{-8} s), and therefore reveal blocked particles, (2) quadrupole doublets formed by paramagnetic particles whose relaxation times are shorter than the Mössbauer measurement time window (10^{-8} s), and (3) Zeeman sextuplets with wide lines whose relaxation times are intermediate. Thus obtained curves $P(H_{\text{eff}})$ make it possible to find MS components and make conclusions on whether these components refer to the corresponding iron oxides and positions of Fe ions in the lattice [2–6,17–20,33–37].

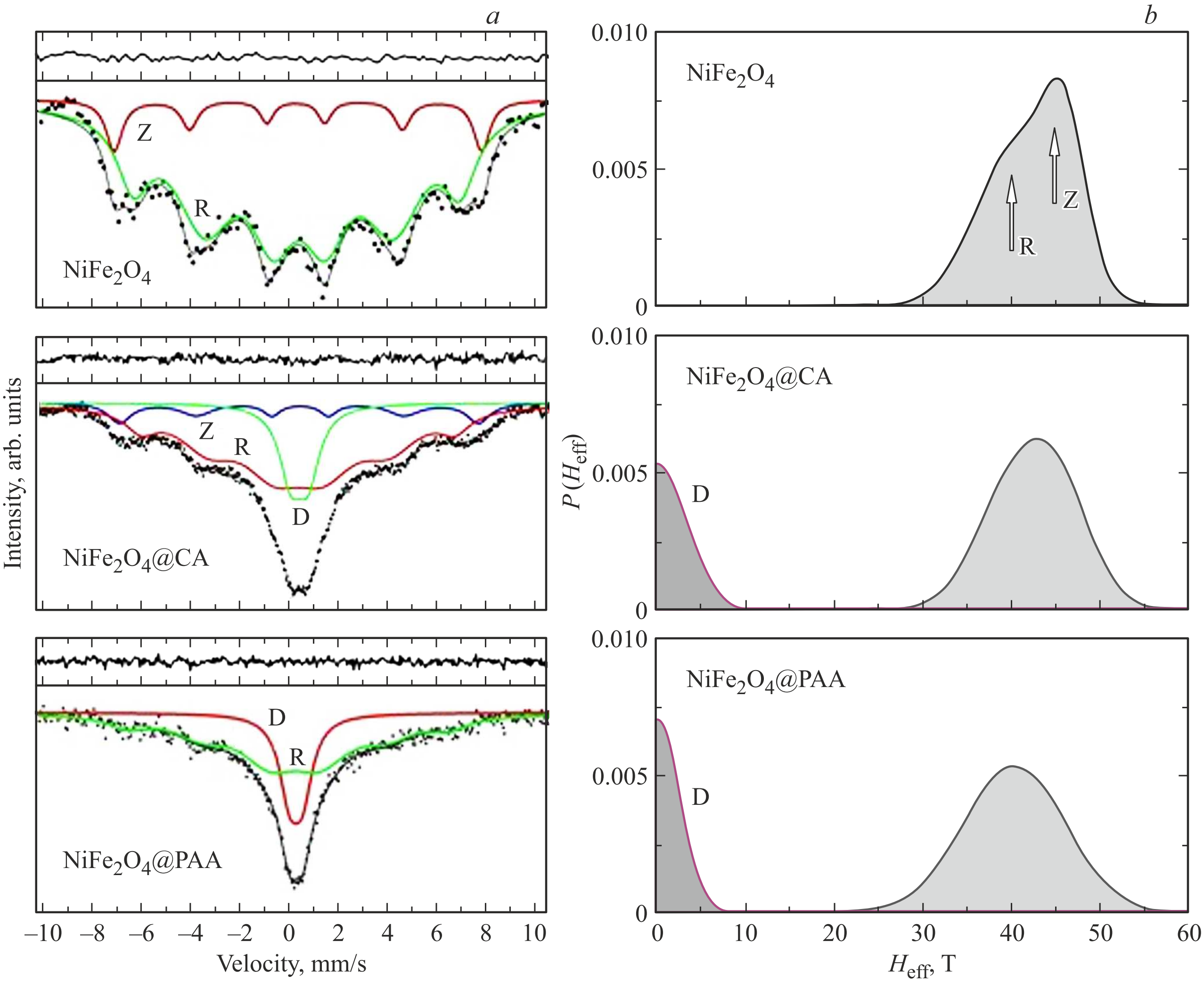

Figure 2. (*a*) — Experimental Mössbauer spectra of $NiFe_2O_4$, $NiFe_2O_4$@CA and $NiFe_2O_4$@PAA MNP at room temperature and their model representations. Sextuplet denoted as *Z* indicates Fe particle ions in a magnetic-ordered state, *R* are Fe ions in superparamagnetic particles, *D* Fe particle ions in the paramagnetic phase. (*b*) — Functions $P(H_{eff})$ recovered from the experimental Mössbauer spectra of $NiFe_2O_4$, $NiFe_2O_4$@CA and $NiFe_2O_4$@PAA MNP using the program [38].

To obtain quantitative information about the values of ultrafine interactions, the experimental $NiFe_2O_4$ MNP MS (Figure 2, *a*) were processed using individual models for each coating that differed in the number of partial sextuplets and doublets. The accuracy of fitting the model spectra to the experimental data is defined by the deviation of experimental data from models (χ^2) which in our cases is in the range from 1.1 to 1.2. Such values of χ^2 indicate a good coincidence between the models and experimental data and, consequently, the reliability of such processing of the obtained spectra. Model spectra obtained by the mathematical analysis of experimental spectra using the program [38] are shown by solid lines. Using the absorption line positions on the velocity scale, ultrafine interaction (UFI) parameters were calculated, i. e. isomeric shifts (IS), quadrupole splitting (QS), effective magnetic fields (H_{eff}) given in Table 2. The isomer shifts (IS) are shown with respect to the α-Fe metal foil. These tables also show the component areas (In) indicating the number of Fe ions in their respective positions.

MS reliably identifies spectral lines belonging to Fe^{2+} and Fe^{3+} ions by their chemical shifts equal to $\sim 0.2{-}0.5$ mm/s for Fe^{3+} and $\sim 0.9{-}1.1$ mm/s for Fe^{2+} [48]. However, for the spinel ferrite MNP, the IS values belonging to Fe ions in the high-spin state Fe^{3+} are usually within the range of 0.3–0.6 mm/s [36]. There are no higher values of the chemical shifts (from 0.9 to 1.1 mm/s), which belong to Fe ions in the low-spin state of Fe^{2+} As can be seen from Table 2, IS values are in the range of 0.3–05 mm/s. This means that in the studied MNP (Figure 3, *a*), there are only iron ions in the high-spin state of Fe^{3+}.

Figure 2, *a* shows that uncoated $NiFe_2O_4$ MNP MS consist of two sextuplets. Intensity of sextuplet (marked

Table 2. UFI parameters for $NiFe_2O_4$, $NiFe_2O_4$@CA and $NiFe_2O_4$@PAA MNP determined from the Mössbauer spectra: Zeeman sextuplet (Z), superparamagnetic component (R) and paramagnetic doublet (D). Line widths (G_1), isomer shifts (IS), quadrupole splitting (QS), effective magnetic fields (H_{eff}) and component areas (In), calculated from the experimental MNP MS

Sample	Comp	G_1 (mm/s)	IS (mm/s)	Q_S (mm/s)	$H_{\text{eff}}(T)$	I_n (%)
$NiFe_2O_4$	Z	0.772 ± 0.259	0.298 ± 0.048	0.084 ± 0.099	46.21 ± 0.41	10
	R	1.575 ± 0.276	0.341 ± 0.045	0.091 ± 0.074	41.09 ± 0.82	90
$NiFe_2O_4$@CA	Z	1.121 ± 0.126	0.342 ± 0.023	0.045 ± 0.048	45.04 ± 0.24	8
	R	1.476 ± 0.162	0.294 ± 0.020	0.028 ± 0.033	39.45 ± 0.42	72
	D	1.124 ± 0.068	0.335 ± 0.008	0.701 ± 0.021	–	18
$NiFe_2O_4$@PAA	R	1.891 ± 0.685	0.116 ± 0.083	0.256 ± 0.145	40.42 ± 1.01	72
	D	0.998 ± 0.161	0.292 ± 0.015	0.522 ± 0.050	–	28

with Z in Figure 2, a), according to the calculations, is 10% of the total spectrum area (see Table 2), effective magnetic field is equal to 46.21 ± 0.41 T. Widths ofZ component lines (0.772 ± 0.259 mm/s) are 3 times as large as the natural width of the Mössbauer line for Fe^{57}, which may be explained by the contributions to the sextuplet made by the Zeeman lines of Fe ions occupying octahedral and tetrahedral ferrite-spinel sublattices. Intensity of component (R) is much higher and is equal to 90% of the total spectrum area (see Table 2), effective field 41.09 ± 0.82 T, and considerably wide lines (1.575 ± 0.276 mm/s). All of this indicates the relaxation nature of (R). MS of ferrite spinels are known to consist of two ZS belonging to Fe ions that occupy two non-equivalent positions in the spinel lattice [48]. Based on $P(H_{\text{eff}})$ for $NiFe_2O_4$ MNP (Figure 2, b), it is also safe to say that Z and R are related to Fe ions located in two non-equivalent positions. However, the width of sextuplet lines Z indicates a magnetic-ordered state of some particles in the sample. Significantly wider lines and shape of R indicate that this component has a relaxation form and belongs to Fe ions located in particles in the superparamagnetic state. Hence, it is suggested that conglomerates of two types of particles are formed in the $NiFe_2O_4$ MNP sample: 1 — coarser magnetic-ordered MNP, 2 — finer particles displaying superparamagnetic properties.

Acid coating of $NiFe_2O_4$ MNP, as shown in Figure 2, a, leads to significant alterations of the MS shape. Thus, coating of $NiFe_2O_4$ MNP with citric acid (CA) leads to a slight intensity reduction of lines and effective magnetic fields of sextuplet Z. Intensity of R lines also decreases and doublet lines appear indicating that paramagnetic phase particles are present in the sample.

On the MS of $NiFe_2O_4$ MNP coated with polyacrylic acid (PAA), intensity of R lines remain unchanged, but the lines became wider. There is no Zeeman component Z, and the intensity of the paramagnetic doublet D has grown.

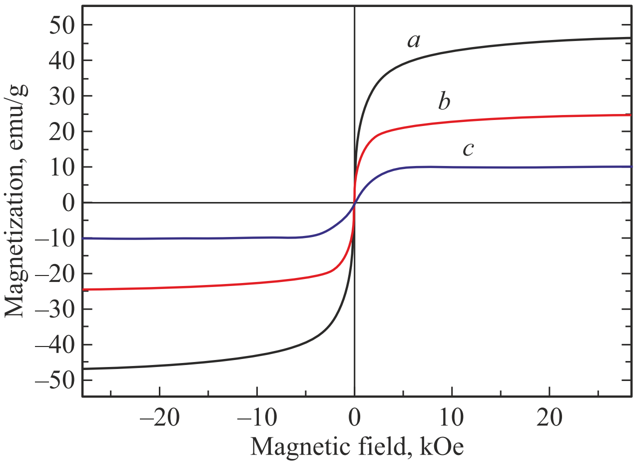

Figure 3. MNP saturation magnetization dependences (a) — $NiFe_2O_4$, (b) — $NiFe_2O_4$@CA and (c) — $NiFe_2O_4$@PAA.

Variations of $P(H_{\text{eff}})$ (Figure 3, b) calculated from the experimental MS of $NiFe_2O_4$ MNP (Figure 2, a) support the conclusions based on the MS transformation (Figure 3, a).

Variation of the MNP MS shape depending on the type of coating may be explained as follows. In case of uncoated $NiFe_2O_4$ MNP, particles are interconnected through strong interactions, thus, forming agglomerates with properties of coarse, medium and fine particles. Citric acid coating of nanoparticles leads to a destruction of agglomerates, formation of particles that don't interact with each other due to CA surface layer and display their real properties of superparamagnetic particles.

Molecular weight and density of polyacrylic acid (PAA) is higher than those of citric acid, moreover, PAA forms firm complexes with transition metal ions. Therefore, PAA coating leads to more considerable, compared with CA, destruction of agglomerates in $NiFe_2O_4$ MNP and formation of more $NiFe_2O_4$ particles separated by PAA coating, as a consequence, the increasing number of $NiFe_2O_4$@PAA

MNP display superparamagnetic and paramagnetic properties.

The mean blocking temperature (T_B) in the Mössbauer experiments is defined as a temperature at which: 1 — a half of magnetic moments of all Fe atoms are fixed in space within the measurement time scale, and 2 — the other half of moments fluctuate giving a pure zero value of the effective field.

MS for state (1) consists of the Zeeman sextuplets (blocked behavior), and state (2) is observed on MS in the form of paramagnetic doublet or singlet line (unblocked behavior) [49,50]. On the MS of $NiFe_2O_4$ MNP (Figure 2, *a*), doublets indicating the particle paramagnetism are not observed. When $NiFe_2O_4$ MNP are coated with citric acid (CA), doublet lines occur on MS, whose areas are much smaller than ZS areas, indicating that the blocking temperature of these particles is higher than 300 K. In case of PAA coated $NiFe_2O_4$ MNP, doublet line intensities grew much higher, indicating that blocking temperature of these particles approached 300 K. Application of the coating leads to reduction of the blocking temperature, which agrees with the conclusions in [51].

Both $NiFe_2O_4$ MNP and SiO_2 coated MNP are core-shell particles as specified in [33]. The magnetic-ordered core is surrounded by a thin surface layer or shell, magnetic moments in which are unordered or beveled with respect to the moment orientation in the particle core. Such shell is formed due to lower, than in the particle core, superexchange interactions of Fe ions located in the surface layer [2–6].

3.3. Findings of the magnetic property investigations

Magnetization variations depending on the magnetic field ($M-H$) of $NiFe_2O_4$@CA and $NiFe_2O_4$@PAA samples obtained in the external magnetic field range from -50 kOe to $+50$ Oe are shown in Figure 3. Figure 3 shows that dependences of magnetization on magnetic field at room temperature are nonlinear both for $NiFe_2O_4$ MNP and CA/PAA coated MNP. Saturation magnetizations (M_s), residual magnetizations (M_r) and coercive forces (H_c) measured at room temperature (300 K) are shown in Table 3, where it can be seen that the type of material affects considerably the magnetic properties of $NiFe_2O_4$ MNP. Saturation magnetization (M_s) equal to 47 emu/g for $NiFe_2O_4$ (Table 1) decreases to 10.1 emu/g with increasing density of coating material for $NiFe_2O_4$@PAA. The residual magnetizations (M_r) of the samples are negligible, and the coercivity (H_c) varies from 9 Oe to 19 Oe. This indicates the homogeneity of the studied superparamagnetic phase particles.

Relation of the residual magnetization (M_r) and saturation magnetization (M_s) defines the hysteresis loop rectangularity (HLR). In accordance with the Stoner–Wohlfarth theory for single-domain structures with uniaxial and cubic anisotropy, theoretical HLR limits are equal to 0.50 and 0.83 [1]. The obtained HLR values (Table 3) correspond to the superparamagnetic state of the studied particles. HLR values are lower than 0.5 (Table 3), which may be associated with the disordering effects or canting of magnetic spin structures in the MNP surface layer.

Table 3. Magnetic properties of $NiFe_2O_4$ MNP at 300 K for various coatings

Sample	M_s (emu/g)	M_r (emu/g)	H_c (Oe)	SQR (M_r/M_s)
$NiFe_2O_4$	47	0.75	9.3	0.0161
$NiFe_2O_4$@CA	26.4	0.24	12.3	0.0098
$NiFe_2O_4$@PAA	10.1	0.11	19.0	0.0206

4. Evaluation of MNP sizes according to the Mössbauer spectroscopy data

Sizes of the studied MNP may be evaluated through comparison of the results with the published Mössbauer data for $NiFe_2O_4$ particles. The Mössbauer spectroscopy data obtained for $NiFe_2O_4$ particles with different sizes indicate that the MS of $10-12$ nm particles against the ZS background has a quadrupole doublet, and with an increase in particle size, the intensity of the ZS lines increases. Thus, in [26,28,40–42,44–54], Mössbauer examination results are shown both for uncoated and coated $NiFe_2O_4$ MNP with sizes from 3 nm to 98 nm. MS of $NiFe_2O_4$ MNP with sizes from 3 nm to 10 nm obtained in [28] are similar to those shown in Figure 3, *a*.

Analysis of the obtained experimental MS and comparison with MS available in the literature suggests that the sizes of the synthesized MNP are in the order of $9-12$ nm, which agrees with the XRD data.

5. Conclusion

Magnetic $NiFe_2O_4$ nanoparticles were synthesized by the hydrothermal technique and then functionalized with polyacrylic acid (PAA) or citric acid (CA). Comprehensive studies of the properties of the synthesized $NiFe_2O_4$ MNP and of the effect of acid functionalization of the particles were conducted using XRD, magnetic and Mössbauer measurements. X-ray diffraction patterns and Mössbauer spectra showed that the synthesized MNP were single-phase and free from foreign impurities. The magnetic measurement data has shown that the studied MNP are in the superparamagnetic state, which was directly confirmed by the Mössbauer measurements. Coating of MNP reduces the blocking temperature (TB), with TB of PAA-coated MNP lower than that of CA-coated MNP. This is explained by the fact that the density and molecular weight of PAA is higher than that of CA leading to higher isolation of between the particles, decrease in the particle agglomeration and removal of particle interaction.

Thus, the use of $NiFe_2O_4$ MNP demonstrates that modification and surface functionalization of particles and creation of new multifunctional biocompatible materials are possible for miscellaneous biomedical applications, in particular, drug delivery and magnetic hyperthermia. The synthesized $NiFe_2O_4$ MNP are superparamagnetic at room temperature, which is the key requirement for particles used for magnetic particle imaging, an advanced human disease diagnosis technique.

Acknowledgments

N. Dogan is grateful to the Council for Scientific and Technological Research of Turkey for supporting his work (grant TUBITAK No: 115E776).

Conflict of interest

The authors declare that they have no conflict of interest.

References

[1] M. Irfan, N. Dogan, A. Bingolbali, F. Aliew. J. Magn, Magn. Mater. **537**, 168150 (2021). https://doi.org/10.1016/j.jmmm.2021.168150.

[2] N. Dogan, O.M. Dogan, M. Irfan, F. Ozel, A.S. Kamzin, V.G. Semenov, I.V. Buryanenko, J. Magn. Magn. Mater. **561**, 169654 (2022).

[3] A.S. Kamzin, G. Caliskan, N. Dogan, A. Bingolbali, V.G. Semenov, I.V. Buryanenko. Phys. Sol. State, **64**, *10*, 1550 (2022). DOI: 10.21883/PSS.2022.10.54249.391

[4] A.S. Kamzin, N. Dogan, O.M. Dogan, V.G. Semenov. Phys. Solid State, **65**, *8*, 1373 (2023). DOI: 10.21883/PSS.2023.08.56587.127

[5] N. Dogan, G. Caliskan, M. Irfan. J Mater Sci: Mater Electron **34**, 390 (2023). https://doi.org/10.1007/s10854-022-09799-x

[6] A.S. Kamzin, V.G. Semenov, L.S. Kamzina. Phys. Solid State, **66**, *7*, 1183 (2024). DOI: 10.61011/PSS.2024.07.58996.74

[7] B. Gleich, J. Weizenecker, Nature. **435**, 1214 (2005). https://doi.org/ 10.1038/nature03808

[8] B. Gleich, Method of determining the spatial distribution of magnetic particles, Google Patents, 2010, US7778681B2.

[9] Gleich, J. Weizenecker, H. Timminger, C. Bontus, I. Schmale, J. Rahmer, J. Schmidt, J. Kanzenbach, J. Borgert, inProc. ISMRM, **18**, 1920 (2010).

[10] W. Li, X. Jia, L. Yin, Z. Yang, H. Hui, J. Li, W. Huang, J. Tian, S. Zhang. iLIVER **1**, 237 (2022). https://doi.org/10.1016/j.iliver.2022.10.003

[11] L.C. Wu, Y. Zhang, G. Steinberg, H. Qu, S. Huang, M. Cheng, T. Bliss, F. Du, J. Rao, G. Song, L. Pisani, T. Doyle, S. Conolly, K. Krishnan, G. Grant, M. Winter. Am J. Neuroradiol. **40**, 206 (2019). https://doi.org/10.3174/ajnr.A5896

[12] M.I. Anik, M.K. Hossain, I. Hossain, A.M.U.B. Mahfuz, M.T. Rahman, I. Ahmed. Nano Select **2**, *6*, 1146 (2021). DOI: 10.1002/nano.202000162

[13] G.F. Stiufiuc, R.I. Appl. Sci. **14**, 1623 (2024). https://doi.org/10.3390/app14041623

[14] N. Panagiotopoulos, R.L. Duschka, M. Ahlborg, G. Bringout, C. Debbeler, M. Graeser, C. Kaethner, K. Lüdtke-Buzug, H. Medimagh, J. Stelzner, T.M. Buzug, J. Barkhausen, F.M. Vogt, J. Hägele. Int. J. Nanomedicine **10**, 3097 (2015). https://doi.org/10.2147/ijn.S70488

[15] B. Rezaei, Z.W. Tay, S. Mostufa, O.N. Manzari, E. Azizi, S. Ciannella, H.-E-J. Moni, C. Li, M. Zeng, J. Gómez-Pastora, K. Wu. Nanosca. **16**, 11802 (2024). DOI: 10.1039/d4nr01195c

[16] C. Lu, L. Han, J. Wang, J. Wan, G. Song, J. Rao. Chem. Soc. Rev. **50**, 8102 (2021). https://doi.org/10.1039/D0CS00260G

[17] G.M. Abilkosomova, D.M. Aronbaev, S.D. Aronbaev. NEORGANICHESKAYA KHIMIYA. Universum: khimiya i biologiya elektron, nauchn. zhurn. **4**, 55 (2024). (in Russian). DOI: 10.32743/UniChem.2024.118.4.17194

[18] J.W.M. Bulte. Adv. Drug Deliv. Rev. **138**, 293 (2019). https://doi.org/10.1016/j.addr.2018.12.007

[19] B. Gleich, J. Weizenecker, J. Borgert. Phys. Med. Biol. **53**, N81 (2008).

[20] B. Rezaei, P. Yari, S.M. Sanders, H. Wang, V.K. Chugh, S. Liang, S. Mostufa, K. Xu, J.-P. Wang, J. Gómez-Pastora, Small. **20**, 2304848 (2023). DOI: 10.1002/smll.202304848

[21] K.S. Joshy, R. Augustine, A. Mayeen, S.M. Alex, A. Hasan, S. Thomas, H. Chi. New J. Chem. **44**, 18162 (2020). DOI: 10.1039/d0nj01163k

[22] X. Lasheras, M. Insausti, I.G. de Muro, E. Garaio, F. Plazaola, M. Moros, L. De Matteis, J.M. de la Fuente, L. Lezama. J. Phys. Chem. C **120**, 3492 (2016). DOI: 10.1021/acs.jpcc.5b10216

[23] M.N. Ahmad, H. Khan, L. Islam, M.H. Alnasir, S.N. Ahmad, M.T. Qureshi, M.Y. Khan. J. Mater. Phys. Sciences **4**, 32 (2023). https://doi.org/10.52131/jmps.2023.0401.0034

[24] A. Muthusamy, M. Arunkumar, N. Kannapiran, S.S. Meena, S.M. Yusuf. J. Mater. Sci: Mater Electron **28**, 15754 (2017). DOI: 10.1007/s10854-017-7468-3

[25] S.B. Narang, K. Pubby. J. Magn. Magn. Mater. **519**, 167163 (2021). https://doi.org/10.1016/j.jmmm.2020.167163

[26] M.H. Sousa, E. Hasmonay, J. Depeyrot, F.A. Tourinho, J.-C. Bacrib, V.E. Dubois, R. Perzynski, Yu.L. Raikher. J. Magn. Magn. Mater. **242–245**, 572 (2002). https://doi.org/10.52131/jmps.2023.0401.0034

[27] M.A.S. Amulya, H.P. Nagaswarupa, M.R.A. Kumar, C.R. Ravikumar, S.C. Prashantha, K.B. Kusuma. App. **1**, 100023 (2020). https://doi.org/10.1016/j.apsadv.2020.100023

[28] U. Kurtan, H. Güngüneş, H. Sözeri, A. Baykal. Ceram. Internat. **42**, 7987 (2016). http://dx.doi.org/10.1016/j.ceramint.2016.01.200

[29] L.M. Sanchez, D.A. Martin, V.A. Alvarez, J.S. Gonzalez. Colloids Surf., A **543**, 28 (2018). https://doi.org/10.1016/j.colsurfa.2018.01.050

[30] A.S. Kamzin, G. Caliskan, N. Dogan, A. Bingolbali, V.G. Semenov, I.V. Buryanenko. Technical Phys., 2022, **67**, *12*, 1640 (2022). DOI: 10.21883/TP.2022.12.55201.152-22

[31] M.E. de Sousa, M.B.F. van Raap, P.C. Rivas, P.M. Zelis, P. Girardin, G.A. Pasquevich, J.L. Alessandrini, D. Muraca, F.H. Sanchez. J. Phys. Chem. C **117**, 5436 (2013). DOI: dx.doi.org/10.1021/jp311556b

[32] M.A. Dheyab, A.A. Aziz, M.S. Jameel, O.A. Noqta, P.M. Khaniabadi, B. Mehrdel. Scient. Rep. **10**, 10793 (2020). https://doi.org/10.1038/s41598-020-67869-8

[33] E. Umut, M. Coşkun, H. Güngüneş, V. Dupuis, A.S. Kamzin. J. Supercond. Novel Magn. **34**, 913 (2021). DOI: 10.1007/s10948-020-05800-y

[34] Mossbauer Spectroscopy Applied to Magnetism and Materials Science. Vol. 1. Ed. G.J. Long, F. Grandjean, Springer Science+Business Media New York 1993. 479 c.

[35] V. Kuncser, O. Crisan, G. Schinteie, F. Tolea, P. Palade, M. Valeanu, G. Filoti. Modern Trends in Nanoscience, vol. 197. Editura Academiei Romane, Bucharest, 2013.

[36] A.S. Kamzin, I.M. Obaidat, V.G. Semenov, V. Narayanaswamy, I.A. Al-Omari, B. Issa, I.V. Buryanenko. Phys. Sol. State. **64**, *6*, 714 (2022). DOI: 10.21883/PSS.2022.06.53838.298.

[37] A.S. Kamzin, I.M. Obaidat, A.A. Valliulin, V.G. Semenov, I.A. Al-Omari. Phys. Sol. State, **62**, **10**, *10*, 1933 (2020). DOI: 10.1134/S1063783420100157

[38] V.G. Semenov, V.V. Panchuk. Programma obrabotki messbauerovskikh spectrov MossFit. Chastnoe soobshchenie. (in Russian).

[39] D.-H. Chen, X.-R. He. Mater. Res. Bull. **36**, 1369 (2001).

[40] R. Malik, S. Annapoorni, S. Lamba, V.R. Reddy, A. Gupta, P. Sharma, A. Inoue. J. Magn. Magn. Mater. **322**, 3742 (2010). doi: 10.1016/j.jmmm.2010.07.019

[41] L.K. Bogart, I.G. Morozov, I.P. Parkin, M.V. Kuznetcov. J. Mater. Sci.: Mater. Electron. **29**, 14347 (2018). https://doi.org/10.1007/s10854-018-9569-z

[42] J. Jacob, M.A. Khadar. J. Appl. Phys. **107**, 114310 (2010). http://dx.doi.org/10.1063/1.3429202.

[43] U. Holzwarth, N. Gibson. Nature Nanotechnology **6**, 534 (2011).

[44] M. Siddique, N.M. Butt. Physica B **405**, 4211 (2010). doi: 10.1016/j.physb.2010.07.012.

[45] V. Sepelak, I. Bergmann, A. Feldhoff, P. Heitjans, F. Krumeich, D. Menzel, F.J. Litterst, S.J. Campbell, K.D. Becker. J. Phys. Chem. C **111**, 5026 (2007). DOI: 10.1021/jp067620s

[46] A.P. Kazin, M.N. Rumyantseva, V.E. Prusakov, I.P. Suzdalev, Yu.V. Maksimov, V.K. Imshennik, S.V. Novichikhin, A.M. Gas'kov. Neorganich. Mater. **45**, *11*, 1381 (2010). (in Russian).

[47] Magnetic Properties of Fine Particles. Ed. J.L. Dormann, D. Fiorani. Elsevier Science Ltd. Series: North-Holland Delta 2012. 430 p.

[48] S.B. Singh, Ch. Srinivas, B.V. Tirupanyam, C.L. Prajapat, M.R. Singh, S.S. Meena, Pramod Bhatt, S.M. Yusuf, D.L. Sastry. Ceram. Internat. **42**, 19188 (2016). http://dx.doi.org/10.1016/j.ceramint.2016.09.081

[49] E. Lima, A.L. Brandl, A.D. Arelaro, G.F. Goya. J. Appl. Phys. **99**, 083908 (2006).

[50] J.M.D. Coey. Phys. Rev. Lett. **27**, 1140 (1971).

[51] S. Morup, C.A. Oxborrow, P.V. Hendriksen, M.S. Pedersen, M. Hanson, C. Johansson. J. Magn. Magn. Mater. **140–144**, 409 (1995). https://doi.org/10.1016/0304-8853(94)00963-5

[52] M. Menzel, V. Sepelak, K.D. Becker. Sol. St. Ionics. **141**, 663 (2001).

[53] A. Bajorek, C. Berger, M. DulskI, M. Zubko, S. Lewinska, K. PrusiK, A.S. Lawska-Waniewska, F. Grasset, N. Randrianantoandro. Metallurg. Mater. Transac. A **53A**, 1208 (2022). https://doi.org/10.1007/s11661-021-06567-0

[54] B. Pacakova, S. Kubickova, G. Salas, A. Mantlikova, M. Marciello, M.P. Morales, D. Niznansky, J. Vejpravova. Nanoscale **9**, 5129 (2017). DOI: 10.1039/x0xx00000x

Translated by E.Ilinskaya